Global gyrokinetic simulations of TEM microturbulence

Global gyrokinetic simulations of TEM microturbulence

T Vernay[1]**, S Brunner**[1]**, L Villard**[1]**, B F McMillan**[2]**, S Jolliet**[1]**, A Bottino**[3]**,
T Görler**[3] **and F Jenko**[3]

[1] Centre de Recherches en Physique des Plasmas, Ecole Polytechnique Fédérale de Lausanne (EPFL),
Association EURATOM–Confédération Suisse, CH-1015 Lausanne, Switzerland
[2] Centre for Fusion, Space and Astrophysics, Department of Physics, University of Warwick, Coventry
CV4 7AL, UK
[3] Max-Planck-Institut für Plasmaphysik, Boltzmannstrasse 2, EURATOM Association, D-85748
Garching, Germany

E-mail: thibaut.vernay@epfl.ch

Abstract
Global gyrokinetic simulations of electrostatic temperature-gradient-driven
trapped-electron-mode (TEM) turbulence using the δf particle-in-cell code ORB5 are
presented. The electron response is either fully kinetic or hybrid, i.e. considering kinetic
trapped and adiabatic passing electrons. A linear benchmark in the TEM regime against the
Eulerian-based code GENE is presented. Two different methods for controlling the numerical
noise, based, respectively, on a Krook operator and a so-called coarse-graining approach, are
discussed and successfully compared. Both linear and non-linear studies are carried out for
addressing the issue of finite-ρ^*-effects and finite electron collisionality on TEM turbulence.
Electron collisions are found to damp TEMs through the detrapping process, while
finite-ρ^*-effects turn out to be important in the non-linear regime but very small in the linear
regime. Finally, the effects of zonal flows on TEM turbulence are briefly considered as well
and shown to be unimportant in the temperature-gradient-driven TEM regime. Consistently,
basically no difference is found between linear and non-linear critical electron temperature
gradients in the TEM regime.

(Some figures may appear in colour only in the online journal)

1. Introduction

Microturbulence is widely believed to be responsible for
anomalous transport in tokamak plasmas. Realistic tokamak
parameters appear to lead to mixed ion-temperature-gradient
(ITG) and trapped-electron-mode (TEM) turbulence. The
adiabatic electron model, although very efficient from the
practical point of view of computer resources, is not always
applicable since the adiabatic assumption does not hold for
trapped electrons nor for passing electrons located at low
order mode rational flux surfaces (i.e. where the safety factor
is rational: $q_s = m/n$, m and n being integers) [1–3]. In
particular, the adiabatic electron model does not allow the
addressing of the electrostatic TEMs nor the electromagnetic
instabilities. The hybrid electron model, briefly explained
in this paper and designed for studying electrostatic TEM

instabilities by providing a kinetic trapped electron response,
was implemented quite early in the development of the
ORB5 code, but only a few collisionless results have been
published before this paper [4–6]. Note that the hybrid
model has the main advantage of allowing larger time steps
for TEM simulations compared with fully kinetic electron
simulations, by a factor corresponding roughly to the ratio
between the electron transit frequency ω_{te} and the electron
bounce frequency ω_{be}: $\omega_{te}/\omega_{be} = 1/\sqrt{\epsilon}$, where $\epsilon = r/R_0$
is the local inverse aspect ratio. Moreover, the hybrid model
prevents electrostatic shear Alfvén waves [7] from appearing
and thus relaxes the corresponding constraint on the time step.
Note that thorough and reliable TEM studies with a global
gyrokinetic code, requiring the evolution of both kinetic ions
and electrons, are very challenging computationally due to the
multiple time and length scales involved in such multi-species

simulations. As a consequence, very few global results have been published so far.

One of the major questions regarding the physics of TEM microturbulence is the importance of zonal flows in the turbulence saturation mechanism. The answer to this question remains complex and not fully understood. Non-linear global simulations of collisionless electrostatic TEM turbulence at $\eta_e = \nabla \ln T_e / \nabla \ln n_e \simeq 3.1$ obtained using ORB5 are described in [6], emphasizing a moderate role of zonal flows in the saturation mechanism of non-linear temperature-gradient-driven TEM instabilities, in agreement with flux-tube (local) results obtained using the GENE code, see [8]. This latter result has recently been confirmed by other local simulations, stating that zonal flows only have an important saturation effect at $\eta_e \lesssim 1$ [9]. Recent global simulations tend to show that zonal flows may constitute an important saturation mechanism in the case $T_e = T_i$ [10]. The importance of the parameter range in determining the efficiency of turbulence saturation by zonal flow shearing has been pointed out in [11] as well. For $\eta_e \gtrsim 1$, an alternative TEM saturation mechanism through perpendicular particle diffusion is proposed in [12]. Note that a non-diffusive component in the electron heat flux due to TEM turbulence is obtained in [13].

In this paper, we first address some important numerical issues related to the δf PIC algorithm applied to global collisional gyrokinetic TEM simulations. In particular, the relevance of the different noise-control procedures available for a PIC code, both in collisionless and collisional configurations, is discussed. Different physical cases are considered, featuring either a pure TEM spectrum or a TEM-dominated spectrum. From a physical point of view, the role of zonal flows in TEM simulations is studied, as well as collisional effects and finite-ρ^*-effects on TEM turbulence.

This paper is organized as follows: section 2 presents the simulation model as well as the numerical methods used by ORB5, which have been shown to satisfy energy consistency [14]. Section 3 provides information about the physical systems that are considered, along with some code diagnostics. Section 4 shows results related to TEM benchmarks performed against the global Eulerian-based gyrokinetic code GENE [15]. Section 5 compares two different methods for controlling the numerical noise in PIC codes. Section 6 investigates the effects of plasma size on TEM dynamics. The effects of axisymmetric potential perturbations (i.e. zonal flows and geodesic acoustic modes) on TEM turbulence are briefly addressed in section 7 and further linked to TEM critical electron temperature gradient (ETG) in section 8. Results of simulations accounting for collisional electrons in the TEM regime are presented in section 9. Conclusions are drawn in section 10.

2. Simulation model and numerical methods

2.1. δf gyrokinetic equation

Simulations are performed with the global gyrokinetic code ORB5 [16, 17]. The collisional model of ORB5 solves the gyrokinetic equation for the gyro-averaged ion distribution

function $f_i(\vec{R}, v_{||}, \mu, t)$, where $\vec{R}$ is the gyrocentre position, $v_{||}$ is the parallel velocity and $\mu = m v_\perp^2 / 2B$ is the magnetic moment, along with the drift-kinetic equation for the electron distribution function $f_e(\vec{R}, v_{||}, \mu, t)$. A local Maxwellian background f_{LM} is chosen for both species. The ions are considered collisionless for TEM simulations, while the electron collision operator consists of a Lorentz operator for electron–ion collisions and a linearized Landau self-collision operator:

$$\hat{C}(\delta f_e) = C_{ei}[\delta f_e] + C_{ee}[f_{LM,e}, \delta f_e] + C_{ee}[\delta f_e, f_{LM,e}], \quad (1)$$

where $\delta f_e = f_e - f_{LM,e}$ represents the deviation of the full distribution f_e with respect to the local Maxwellian background $f_{LM,e}$. The first term on the right-hand side of equation (1) is the Lorentz operator, representing collisions of electrons on ions in the limit $m_i \gg m_e$. The second term on the right-hand side of equation (1) represents collisions of δf_e on the background $f_{LM,e}$ and the third term represents the background reaction (collisions of $f_{LM,e}$ on δf_e) ensuring the local conservation of density, parallel momentum and kinetic energy. Dropping the electron index for simplicity, the approximated background reaction term is of the form [18, 19]:

$$\frac{C[\delta f, f_{LM}]}{f_{LM}} \simeq \mathcal{B}(\delta f)$$
$$= \frac{1}{n_0} \left\{ 6\sqrt{\pi} H(\mathsf{v}) \frac{\delta \mathcal{P}_{||} v_{||}}{v_{th}^2} + \sqrt{\pi} G(\mathsf{v}) \frac{\delta \mathcal{E}}{v_{th}^2} \right\}, \quad (2)$$

where n_0 is the background density, $v_{th} = \sqrt{T/m}$ is the thermal velocity and $\mathsf{v} = v/v_{th}$. The functions $H(\mathsf{v})$ and $G(\mathsf{v})$ are defined in [20] and related to the Rosenbluth potentials relative to a Maxwellian background. $\delta \mathcal{P}_{||}$ and $\delta \mathcal{E}$ are respectively the changes in the parallel momentum and the kinetic energy of the fluctuation distribution due to $C[f_{LM}, \delta f]$:

$$\delta \mathcal{P}_{||}(\delta f, \vec{R}) = -\int C[f_{LM}, \delta f] v_{||} d^3 v, \quad (3)$$

$$\delta \mathcal{E}(\delta f, \vec{R}) = -\int C[f_{LM}, \delta f] v^2 d^3 v. \quad (4)$$

The form (2) ensures the same symmetry properties as the exact background reaction term and associated properties (H-theorem, conservation properties and stationary states).

A source term S is also considered for both ions and electrons, such that the ion gyrokinetic equation and the electron drift-kinetic equation read, respectively:

$$\frac{D\delta f_i}{Dt} = -\frac{D f_{LM,i}}{Dt} + S(\delta f_i), \quad (5)$$

$$\frac{D\delta f_e}{Dt} + C_{ei}[\delta f_e] + C_{ee}[f_{LM,e}, \delta f_e]$$
$$= -\frac{D f_{LM,e}}{Dt} - C_{ee}[\delta f_e, f_{LM,e}] + S(\delta f_e), \quad (6)$$

where D/Dt is the collisionless gyrokinetic (respectively drift-kinetic) operator:

$$\frac{D}{Dt} = \frac{\partial}{\partial t} + \frac{d\vec{R}}{dt} \cdot \frac{\partial}{\partial \vec{R}} + \frac{dv_{||}}{dt} \frac{\partial}{\partial v_{||}}. \quad (7)$$

The gyrokinetic (respectively drift-kinetic) equations of motion for the gyrocentre variables, derived by Hahm [21],

are given by

$$\frac{d\vec{R}}{dt} = \vec{v}_G = v_{||}\hat{b} + \underbrace{\vec{v}_{\nabla B} + \vec{v}_c + \vec{v}_{E \times B}}_{\vec{v}_d}, \quad (8)$$

$$\frac{dv_{||}}{dt} = \frac{1}{mv_{||}}\vec{v}_G \cdot (q\vec{E} - \mu\vec{\nabla}B), \quad (9)$$

$$\frac{d\mu}{dt} = 0, \quad (10)$$

which are valid for small fluctuation levels. Here $\hat{b} = \vec{B}/B$ is the unit vector along $\vec{B}$, $\vec{v}_G$ is the gyrocentre velocity, $\vec{v}_{\nabla B}$ is the ∇B drift velocity, $\vec{v}_c$ is the curvature drift velocity, $\vec{v}_{E \times B}$ is the $\vec{E} \times \vec{B}$ drift velocity and $\vec{E}$ is the gyro-averaged electric field deriving from the electrostatic potential ϕ. Note that for electrons, the electric field at the gyrocentre position is considered instead of the gyro-averaged electric field (drift-kinetic approximation).

2.2. δf particle-in-cell discretization

ORB5 uses the low noise δf particle-in-cell (PIC) method, requiring the introduction of N numerical particles, called markers, for sampling the fluctuation distribution δf of both species. Introducing two weights $w_r(t)$ and $p_r(t)$ for the marker r, the fluctuation distribution δf and associated background distribution f_{LM}, respectively, read:

$$\delta f(\vec{R}, v_{||}, \mu, t) = \sum_{r=1}^{N} \frac{m}{B_{||}^*} w_r(t)\delta[\vec{R} - \vec{R}_r(t)]$$
$$\times \delta[v_{||} - v_{||,r}(t)]\delta[\mu - \mu_r(t)], \quad (11)$$

$$f_{LM}(\vec{R}, v_{||}, \mu) = \sum_{r=1}^{N} \frac{m}{B_{||}^*} p_r(t)\delta[\vec{R} - \vec{R}_r(t)]$$
$$\times \delta[v_{||} - v_{||,r}(t)]\delta[\mu - \mu_r(t)], \quad (12)$$

where $B_{||}^* = B + mv_{||}(\vec{\nabla} \times \hat{b}) \cdot \hat{b}/q$ and r is an index for labelling the N markers. δ stands here for the Dirac function. The weight equations for each species are of the form

$$\frac{d}{dt}w_r(t) = -p_r(t) \left.\frac{1}{f_{LM}}\frac{D}{Dt}f_{LM}\right|_{[z_r(t),t]}$$
$$-p_r(t) \left.\frac{C[\delta f, f_{LM}]}{f_{LM}}\right|_{[z_r(t),t]}, \quad (13)$$

$$\frac{d}{dt}p_r(t) = p_r(t) \left.\frac{1}{f_{LM}}\frac{D}{Dt}f_{LM}\right|_{[z_r(t),t]}, \quad (14)$$

where the last term on the right-hand side of equation (13) is set to 0 for the collisionless ions, while in the case of electrons it represents the background reaction term of the self-collision operator $C_{ee}[\delta f_e, f_{LM,e}]$. Collisional and collisionless dynamics are separately considered through the time splitting approach. Solving the distribution equations for both species is thus performed by integrating numerically in time equations (8)–(10) to obtain the collisionless marker trajectories $z_r(t) = [\vec{R}_r(t), v_{||,r}(t), \mu_r(t)]$ together with weight equations (13) and (14). The collisional marker trajectories for electrons, representing both $C_{ei}[\delta f_e]$ and $C_{ee}[f_{LM,e}, \delta f_e]$ in equation (6), are accounted for through random kicks in velocity space, as described in detail in [20].

Note that the linear runs are performed by dropping terms containing the perturbed electric field in the marker trajectories (equations (8)–(10)).

2.3. Quasi-neutrality equation

The electrostatic approximation is used in our model. Further considering the decomposition $f_i = f_{LM,i} + \delta f_i$, the background ion density n_{i0} is given by the gyrodensity $\bar{n}_{i0}$:

$$n_{i0} \simeq \bar{n}_{i0}(\vec{x}) = \int \frac{B_{||}^*}{m}d^3R\,dv_{||}\,d\mu\,d\alpha\,f_{LM,i}(\vec{R}, v_{||}, \mu)$$
$$\times \delta(\vec{R} + \vec{\rho} - \vec{x}), \quad (15)$$

where α is the gyro-angle and $\vec{\rho}(\mu, \alpha)$ is the Larmor radius vector. One assumes that the background densities of electrons and ions verify quasi-neutrality, i.e. $Z\bar{n}_{i0} = n_{e0}$, where Z is the ion charge. The perturbed ion density has both a perturbed gyrodensity contribution $\overline{\delta n_i}$ as well as a polarization drift term $\delta n_{pol,i}$:

$$\delta n_i(\vec{x}, t) = \overline{\delta n_i} + \delta n_{pol,i}. \quad (16)$$

In ORB5 the polarization drift term $\delta n_{pol,i}$ is both linearized and expanded to second order in $k_{\perp}\rho_{Li}$ (long wavelength approximation), where $k_{\perp}$ is the characteristic perpendicular wavenumber and ρ_{Li} the ion Larmor radius: $\delta n_{pol,i} \simeq \nabla_{\perp} \cdot [(n_{i0}/B\Omega_i)\nabla_{\perp}\phi]$. Note that the polarization drift linearization assumes $|\delta f| \ll f_{LM}$. In the case of drift-kinetic electrons, the following quasi-neutrality equation for the fluctuating components is considered:

$$-\nabla_{\perp} \cdot \left(\frac{n_{i0}(\Psi)}{B\Omega_i}\nabla_{\perp}\phi(\vec{x}, t)\right) = \overline{\delta n_i}(\vec{x}, t) - \frac{1}{Z}\delta n_e(\vec{x}, t), \quad (17)$$

where δn_e is the perturbed electron density, Ω_i is the ion cyclotron frequency and ϕ is the electrostatic potential. Since the electrons are considered drift-kinetic in equation (17), the electron density is in general equal to the electron gyrocentre density.

Within the frame of the so-called hybrid model, the kinetic electron response is computed over the trapped region of phase space, while the passing region is considered adiabatic. The quasi-neutrality equation thus becomes

$$\langle\alpha_p\rangle_S(\Psi)n_{i0}\frac{e[\phi - \langle\phi\rangle_S]}{T_{0e}(\Psi)} - \vec{\nabla}_{\perp} \cdot \left[\frac{n_{i0}}{B\Omega_i}\vec{\nabla}_{\perp}\phi\right]$$
$$= \overline{\delta n_i} - \frac{1}{Z}\delta n_e^{trapped}, \quad (18)$$

where $\langle\alpha_p\rangle_S(\Psi)$ is the local flux-surface-averaged fraction of passing electrons and $\langle\phi\rangle_S$ is the flux-surface-averaged electrostatic potential. The adiabatic response of passing electrons is the first term on the left-hand side of equation (18), while the kinetic response of trapped electrons is the last term on the right-hand side of equation (18). Making use of a finite-element method, the quasi-neutrality equation is solved in straight-field-line magnetic coordinates (s, θ^*, φ), where s is the flux surface label, θ^* is the straight-field-line poloidal angle and φ is the toroidal angle. The considered grid size depends on the $\rho^* = \rho_s/a$ parameter, where ρ_s is the sound Larmor radius and a is the plasma minor radius. The number

of grid points is typically $n_s \times n_{\theta*} \times n_\varphi = 128 \times 512 \times 256$ for $\rho^* = 1/180$ and $n_s \times n_{\theta*} \times n_\varphi = 64 \times 256 \times 128$ for $\rho^* = 1/80, 1/60$. For simulations with fully kinetic electrons, n_s is doubled.

2.4. Sources and noise control

The sources $S = S_k + S_H$ appearing in equations (5) and (6) consist of a Krook operator $S_k = -\gamma_k \delta f + S_{corr}$ and a heating operator

$$S_H = -\gamma_H \left(\widetilde{\delta f}(\Psi, \mathcal{E}, t) - \widetilde{f_{LM}}(\Psi, \mathcal{E}, t) \frac{\int d\mathcal{E} \, \widetilde{\delta f}(\Psi, \mathcal{E}, t)}{\int d\mathcal{E} \, \widetilde{f_{LM}}(\Psi, \mathcal{E}, t)} \right), \tag{19}$$

the symbol $\sim$ standing for the operator which reconstructs the distribution in the $(\Psi, \mathcal{E})$ space, where Ψ is the poloidal magnetic flux and $\mathcal{E}$ the kinetic energy. The details of the source terms are given in [22]. Note that the heat source is built in order to conserve the density, and the zonal flows. Moreover, the Krook operator is built in order to conserve the density, parallel momentum and energy of the considered species, as well as the zonal flows, through the correction term S_{corr}.

The heat source S_H aims at maintaining an effective temperature profile $T = T(\Psi)$, both for ions and electrons. Transport processes indeed tend to relax the temperature profile while source terms tend to readjust it towards the reference background profile. The effective time-averaged profile thus equilibrates more or less near the reference background profile depending on the strength of the relaxation parameter γ_H in the source term. The Krook operator S_k acts as a noise-control operator by applying a small decay of the weights, which allows us to carry out long turbulence simulations with a PIC code such as ORB5. Note that the Krook operator is systematically used in this paper to control the numerical noise associated with the collisionless ions. Typically 100×10^6 markers are used along with the Krook operator. Successful non-linear benchmarks between GENE and ORB5 have already been performed in the ITG regime [23, 24], providing a stringent test for the Krook operator as a noise-control procedure.

The Krook operator is, however, impractical for carrying out collisional simulations, since the required numerical decay rate γ_k which needs to be chosen for the approach to be effective is typically of the order of the collision frequency and may thus significantly interfere with the corresponding physical effects. The control of numerical noise in the presence of collisions is thus handled by making use of the so-called coarse-graining procedure, first proposed in [19] and further simplified in [25]. The implementation of the coarse-graining procedure in the ORB5 code is described in [26]. The idea is to perform a binning of the markers in the 5D gyrokinetic phase space. Periodically (every n_{cg}th time step), the weight of each marker is set to the average weight value of all the markers within the same bin. The size of the bins needs to be carefully chosen, in order to prevent any artificial damping at relevant scales from occurring, both in configuration and velocity space. In configuration space, the number of bins is typically chosen according to the grid for the field solver,

accounting for one major difference: in contrast to the field solver, the binning is performed in the field-aligned coordinates $(s, \theta^*, z = \varphi - q_s \theta^*)$, q_s being the safety factor. These coordinates allow us to take larger bins in the poloidal direction (typically $N_s \times N_{\theta*} \times N_z = 64 \times 32 \times 128$ for $\rho^* = 1/60$), thus improving the statistics of the coarse-graining procedure. In velocity space, the binning is performed in the energy (E)-pitch angle (ξ) space with a number of bins $n_E \times n_\xi \sim 64 \times 64$. The typical number of bins requires more electron markers than the Krook operator in order to control the noise properly, about 300×10^6–600×10^6 markers.

3. Equilibrium profiles and physical cases

The considered *ad hoc* equilibrium [27] consists of a tokamak configuration with circular and concentric magnetic surfaces. In this case, the axisymmetric magnetic field is given by $\vec{B} = \vec{\nabla}\Psi \times \vec{\nabla}\varphi + F(\Psi)\vec{\nabla}\varphi$, assuming $\Psi = \Psi(r)$ with $d\Psi/dr = r B_0/\bar{q}(r)$, as well as $F = R B_\varphi = R_0 B_0$, so that

$$\vec{B} = \frac{B_0 R_0}{R} \left(\hat{e}_\varphi + \frac{r}{R_0 \bar{q}(r)} \hat{e}_\theta \right), \tag{20}$$

where R is the major radius, r is the local minor radius, φ is the toroidal angle, θ is the poloidal angle and $\hat{e}_\varphi$, $\hat{e}_\theta$ are the unit vectors in the toroidal and poloidal directions, respectively. Furthermore, B_0 and R_0 stand for the magnetic field amplitude and major radius on the magnetic axis ($r = 0$). The $\bar{q}$ profile is chosen quadratic: $\bar{q}(r) = \bar{q}_0 + \bar{q}_1 r^2/a^2$ and is related to the safety factor profile $q_s(r)$ by the relation $\bar{q}(r) = \sqrt{1 - \epsilon^2} q_s(r)$. The values $\bar{q}_0 = 0.854$ and $\bar{q}_1 = 2.184$ are chosen such that $\bar{q}(r/a = 0.5) = 1.4$ and the magnetic shear $(r/q_s)dq_s/dr|_{r=0.5a} = \hat{s}(r/a = 0.5) \simeq 0.75$.

Let $\mathcal{A}$ stand for either the temperature T or density n of a given species, and $\kappa_\mathcal{A} = a/L_\mathcal{A}$, where $L_\mathcal{A}$ is the characteristic length of the considered gradient. For non-linear simulations, profiles are defined with respect to the coordinate r, with a flat logarithmic gradient:

$$\frac{d \ln \mathcal{A}}{d(r/a)} = -\frac{\kappa_\mathcal{A}}{2} \left[\tanh \left(\frac{r - (r_0 - \Delta_\mathcal{A})}{\Delta_r} \right) - \tanh \left(\frac{r - (r_0 + \Delta_\mathcal{A})}{\Delta_r} \right) \right], \tag{21}$$

where the values $r_0 = 0.5a$ for the centre of the gradient profile, $\Delta_r = 0.04a$ for the width of the ramps and $\Delta_\mathcal{A} = 0.3a$ for the gradient profile width are chosen. For linear simulations, peaked shape profiles are used:

$$\frac{d \ln \mathcal{A}}{d(r/a)} = -\kappa_\mathcal{A} \cosh^{-2} \left(\frac{r - \tilde{r}_0}{\Delta_\mathcal{A}} \right), \tag{22}$$

with $\tilde{r}_0 = 0.5a$ and $\Delta_\mathcal{A} = 0.2a$ or $\Delta_\mathcal{A} = 0.3a$.

The particle flux Γ and the energy flux Q are given by

$$\Gamma = \left\langle \int \delta f \vec{v}_{E \times B} \cdot \vec{\nabla} r \, d^3 v \right\rangle_S, \tag{23}$$

$$Q = \left\langle \int \delta f \frac{m v^2}{2} \vec{v}_{E \times B} \cdot \vec{\nabla} r \, d^3 v \right\rangle_S, \tag{24}$$

where $\langle \rangle_S$ stands for the flux-surface-average operator. The particle diffusivity is $D = \Gamma / |\nabla n|$, while the energy diffusivity is defined by $\chi^E = Q / n |\nabla T|$. Diffusivities are normalized with respect to the gyro-Bohm units $\rho_s^2 c_s / a$, where $c_s = \sqrt{Z T_e / m_i}$ is the sound speed evaluated at $r/a = 0.5$ and $\rho_s = c_s / \Omega_i$ is the sound Larmor radius evaluated at $r/a = 0.5$ with the magnetic field B_0 on axis. The zonal flow $\vec{E} \times \vec{B}$ shearing rate $\omega_{E \times B}$ is defined as the radial derivative of the radial electric field E_r as follows: $\omega_{E \times B} = (r/q_s B_0) \mathrm{d}/\mathrm{d}r (q_s E_r / r)$ [28], where $E_r = -\mathrm{d} \langle \phi \rangle_S / \mathrm{d}r$.

The standard CYCLONE case [29] features dominant ITG modes at low $k_\theta \rho_i$ and dominant TEM modes at higher $k_\theta \rho_{Li} \sim 1$. This physical situation is a major impediment to CYCLONE TEM studies with ORB5, since the quasi-neutrality solver is only valid for $k_\theta \rho_{Li} \lesssim 1$. In order to study a typical temperature-gradient-driven TEM instability, we define a TEM CYCLONE case, which is the CYCLONE case ($\rho^* = \rho_s / a = 1/180$, deuterium as ion species) with a weaker ion temperature gradient: $R_0 / L_{Ti} = R_0 / L_n = 2.2$, $R_0 / L_{Te} = 6.9$. Here, L_n and L_T are the characteristic lengths of the density and temperature gradients respectively. A smaller case, called the TEM TCV case, is built according to the parameters of the *tokamak à configuration variable (TCV)*. The TEM TCV case considers the same temperature, density and safety factor profiles as the TEM CYCLONE case and keeps the parameters $a/L_n = a/L_{Ti} \simeq 0.8$ and $a/L_{Te} \simeq 2.5$ from the TEM CYCLONE case, along with the geometrical parameters $R_0 = 0.88$ m, $a = 0.25$ m, $B_0 = 1.43$ T and $\rho^* = 1/80$. Moreover, deuterium is also chosen as the ion species. Choosing the parameters of either the TEM CYCLONE case or the TEM TCV case leads to dominant TEM instabilities even at low $k_\theta \rho_{Li}$. Considering some TCV-relevant temperature and density values ($n \sim 10^{19} – 2 \times 10^{19}$ m^{-3} and $T \sim 1$–2.5 keV) provides a range of physical collisionality $\nu_{ei,phys} \sim 5 \times 10^{-3}$–$5 \times 10^{-2} [c_s/a]$. The same range of physical collisionality is obtained for the TEM CYCLONE case, considering relevant DIII-D parameters ($n \sim 2 \times 10^{19}$–3×10^{19} m^{-3} and $T \sim 2$–5 keV). For both cases, the conditions $T_i = T_e$ as well as $T_i < T_e$ are studied.

Note that neither TEM TCV nor TEM CYCLONE cases exhibit a purely temperature-gradient-driven TEM spectrum. Indeed, ETG modes are present at smaller poloidal wavelengths $k_\theta \rho_{Li} \gtrsim 1$, which are not resolved both due to the assumption $k_\theta \rho_{Li} < 1$ of the ORB5 solver and the fact that passing electrons are forced to respond adiabatically in the hybrid electron model used in ORB5, while ETG modes require a kinetic representation for this group of particles. A physical case considered only in section 7, exhibiting a so-called purely temperature-gradient-driven TEM spectrum, i.e. featuring no ETG modes nor density-gradient-driven TEMs, was identified through a parameter scan in the linear regime using the GENE code. This case is characterized by the following physical parameters: CYCLONE case geometry with $T_i / T_e = 0.3$, $R_0 / L_n = 1.0$, $R_0 / L_{Te} = 4.75$, and $R_0 / L_{Ti} = 3.0$. The corresponding linear spectrum is unstable in the range $0 < k_\theta \rho_{Li} \lesssim 0.6$.

Except for the results of section 4 where fully kinetic electrons are used, all other results are obtained within the frame of the hybrid electron model already introduced. Heavy electrons are usually considered ($m_i / m_e = 200$) in order to further facilitate the global simulations presented here. Note that using heavy electrons should be relevant as long as $\omega / \omega_{be} \ll 1$, where ω is the characteristic TEM frequency of the considered system and $\omega_{be} = \sqrt{\epsilon T_e / m_e} / q_s R_0$ is the electron bounce frequency. The time step chosen for TEM simulations performed through the hybrid model is typically $\Delta t \sim 2 \times 10^{-2} [a/c_s]$. Actually, a mass ratio $m_i / m_e = 200$ has been checked to provide converged linear growth rates (within less than 5%) in the frame of TEM simulations using the hybrid model described in this paper (see for instance [6], or figure 3.9 in [30]). Regarding non-linear TEM simulations in the frame of a fully kinetic electron model, a mass ratio $m_i / m_e = 400$ was found to provide electron heat fluxes smaller by $\sim 25\%$ compared with fluxes obtained with the realistic mass ratio [8]. However, the convergence with electron mass is clearly faster within the frame of the hybrid model and there is no significant difference expected in the turbulence level between a simulation with realistic $m_i / m_e = 1836$ hybrid electrons and heavy $m_i / m_e = 200$ hybrid electrons. Using heavy electrons is therefore an approximation but the hybrid model is probably a more significant limitation of the electron model.

4. ORB5-GENE linear TEM benchmark

Considering the TEM CYCLONE case with $T_i = T_e$ and the peaked gradient profiles for density and temperature, as described by equation (22) with $\Delta_{\mathcal{A}} = 0.3a$, a global collisionless linear benchmark in the TEM regime is performed against the global version of the Eulerian-based gyrokinetic code GENE [15]. In contrast to the other results and simulations presented in this paper, fully kinetic electrons of mass $m_i / m_e = 400$ are considered in this section. In the electrostatic approximation, fully kinetic electrons may destabilize electrostatic shear Alfvén modes and thus require small time steps for proper TEM simulations with particles, as explained in [7]. The required time step scales with $\Delta t \sim k_\theta$ and thus needs to be even smaller for simulations considering long poloidal wavelengths. ORB5 uses time steps in the range $\Delta t \sim 5 \times 10^{-4}$–$5 \times 10^{-3} [a/c_s]$ for the considered TEM CYCLONE case with fully kinetic electrons. Due to the above-mentioned numerical challenges, the simulation for the lowest considered value $k_\theta \rho_s = 0.125$ has in fact been performed in the case of ORB5 within the frame of the hybrid model. Figure 1 shows the benchmark results for both the growth rate spectrum and the real frequency spectrum. Note the very good agreement at long wavelengths ($k_\theta \rho_s \lesssim 0.5$) between both codes. Discrepancies at larger $k_\theta \rho_s \gtrsim 0.5$ can probably be attributed to the long wavelength approximation assumed by the ORB5 field solver. The modes $k_\theta \rho_s \gtrsim 0.5$ are in fact not expected to contribute significantly to turbulent heat transport for the considered parameters [31] and the long wavelength approximation in the quasi-neutrality equation should therefore be an appropriate model for the corresponding turbulence simulations presented in this paper. In addition, local (flux-tube) results obtained with GENE are shown in
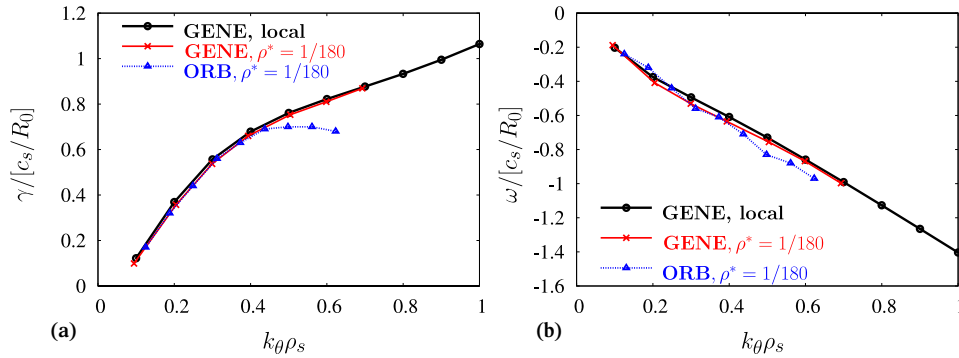
Figure 1. TEM CYCLONE case, $T_e = T_i$. Global simulations for $\rho^* = 1/180$ and fully kinetic electrons (except $k_\theta \rho_s = 0.125$ for ORB5 where hybrid electrons are considered). Linear benchmark in the TEM regime between ORB5 and GENE, providing good agreement regarding (a) the linear growth rate spectrum and (b) the real frequency spectrum for $k_\theta \rho_s \lesssim 0.5$. Discrepancies at larger $k_\theta \rho_s \gtrsim 0.5$ come from the long wavelength approximation assumed by the ORB5 field solver. For comparison, local (flux-tube) simulations obtained with GENE are also shown.
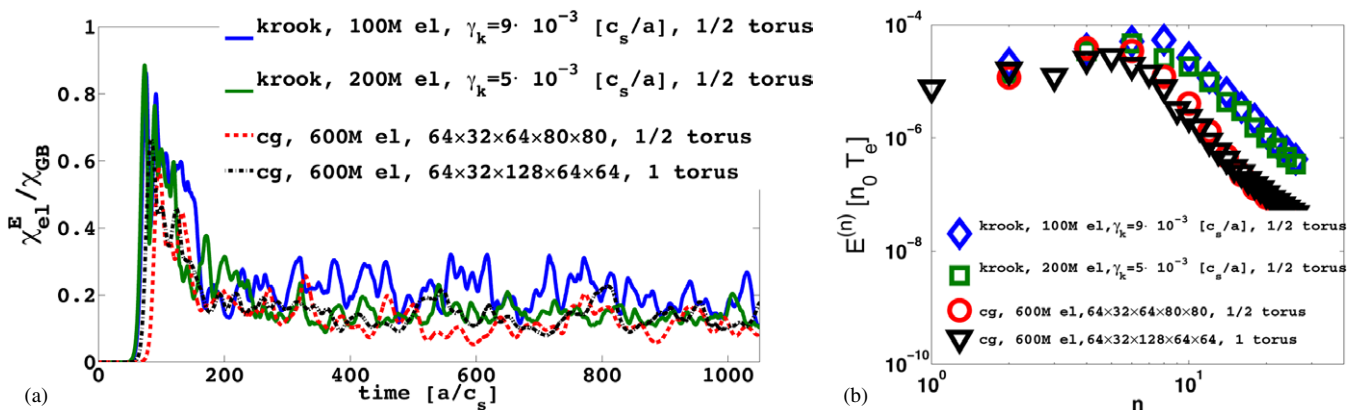
Figure 2. Small TEM CYCLONE case, $T_i = T_e/3$, $\rho^* = 1/60$. (a) Electron energy diffusivity χ_{el}^E averaged between $r/a = 0.2$ and $r/a = 0.8$ compared for different noise-control methods, both Krook operator and coarse-graining (cg), and different numerical parameters. (b) Toroidal mode energy spectrum $E^{(n)}$ averaged between $t = 800[a/c_s]$ and $t = 1050[a/c_s]$. Differences at short wavelengths are observed between the coarse-graining procedure and the Krook operator.

figure 1. Only a very small difference is observed in the linear growth rates and real frequencies between local and global simulations. The weakness of finite-ρ^* effects in linear temperature-gradient-driven TEM simulations is confirmed by ORB5 simulations presented in section 6.

5. Comparison of noise-control methods

In view of carrying out collisional, non-linear simulations it is essential to address the issue of numerical noise. In this section, a comparison of collisionless TEM simulations using different noise-control methods for electrons, either the Krook operator or the coarse-graining as explained in section 2.4, is performed within the frame of the hybrid model. The choice of the coefficient γ_K for the Krook operator, which needs to be significantly smaller (typically 10–20%) than the maximum linear growth rate of the spectrum corresponding to the considered physical system, is naturally important, as well as the coarse-graining parameters. Note that, for a so far unknown reason, TEM simulations require a coarse-graining procedure applied to electrons at each time step in order to maintain a stationary transport level (while applying the coarse-graining every 10th time step is sufficient for ITG

turbulence with adiabatic electrons [26]). At each time step, the electron w-weight is thus set to the average bin value, while the p-weight is unaffected. Moreover, a higher grid resolution in configuration space appears to be required for the coarse-graining binning in TEM simulations. As a consequence, a small plasma is easier to handle for the comparison between the Krook operator and the coarse-graining, due to the fact that a higher grid resolution in configuration space can be afforded. A reduced TEM CYCLONE case is thus chosen, considering $T_i = T_e/3$ and $\rho^* = 1/60$. Non-linear simulations are performed, using either the Krook operator or the coarse-graining (cg) procedure, for different numerical parameters as presented in figure 2(a) showing the electron energy diffusivity χ_{el}^E/χ_{GB} averaged between $r/a = 0.2$ and $r/a = 0.8$. Within the statistical uncertainty range inherent to non-linear simulations, good agreement related to turbulent transport is obtained between the two noise-control methods. Table 1 summarizes the electron energy diffusivity χ_{el}^E/χ_{GB} averaged between $t = 800[a/c_s]$ and $t = 1000[a/c_s]$ for the different cases considered in figure 2(a). However, as shown in figure 2(b) presenting the energy spectrum, the turbulent modes are more damped by the cg procedure in the range of shorter wavelengths ($n \sim 20$ corresponding to $k_\theta \rho_s \sim 1$). Due to

Table 1. Electron energy diffusivity χ_{el}^E/χ_{GB} averaged between $r/a = 0.2$ and $r/a = 0.8$ as well as between $t = 800[a/c_s]$ and $t = 1000[a/c_s]$, for the four different cases presented in figure 2(a). 100 M electron markers are probably not sufficient for a fully converged simulation considering the Krook operator. The Krook coefficients, $\gamma_k = 9 \times 10^{-3}[c_s/a]$ and $\gamma_k = 5 \times 10^{-3}[c_s/a]$, respectively, remain much smaller than the corresponding maximum linear growth rate $\gamma_{max} \sim 0.18[c_s/a]$.

|	Krook, 100 M el.	Krook, 200 M el.	cg, 80×80	cg, 64×64
χ_{el}^E/χ_{GB}	0.18	0.14	0.12	0.14
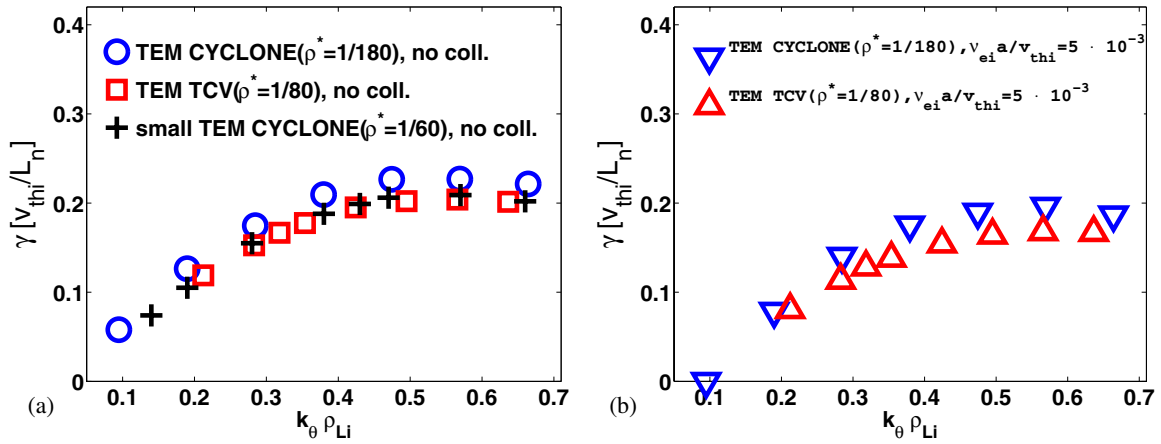
Figure 3. k_θ-spectrum of the linear growth rate γ, for the TEM CYCLONE case ($\rho^* = 1/180$) and the TEM TCV case ($\rho^* = 1/80$) with $T_e = T_i$, considering (*a*) a collisionless case and (*b*) a collisional case. Additional collisionless results related to a small TEM CYCLONE case ($\rho^* = 1/60$, $T_e = T_i$) are shown as well. The influence of plasma size (through ρ^* effects) on TEM linear growth rates turns out to be small, both for the collisionless and the collisional situations. As expected, electron collisions tend to reduce the linear growth rate at each value of $k_\theta\rho_{Li}$.

the limited role of short wavelength modes in the turbulent transport, the electron diffusivity is only marginally affected by the choice of the noise-control method, as already emphasized. Note however that, as already mentioned, the Krook operator is inappropriate for collisional simulations.

## 6. Linear and non-linear ρ^* effects in the TEM regime

The plasma finite-size effects on the turbulence level, appearing through the $\rho^* = \rho_s/a$ parameter in global simulations, turn out to be important both in linear and non-linear ITG regimes, as discussed e.g. in [15, 23, 32, 33]. Global simulations are found to provide lower linear growth rates and turbulent diffusivities than simulations performed in the local flux-tube limit ($\rho^* \to 0$). As an illustration, let us quote results from the standard ITG-dominated CYCLONE case ($\rho^* = 1/180$, $T_i = T_e$, $R/L_{T_i} = R/L_{T_e} = 6.9$, $R/L_n = 2.2$). ORB5 CYCLONE simulations with adiabatic electrons provide a maximum linear growth rate $\gamma_{max}(\rho^* = 1/180) \simeq 0.12[v_{thi}/L_n]$, while the same simulations considering $\rho^* = 1/60$ give a significantly reduced maximum linear growth rate $\gamma_{max}(\rho^* = 1/60) \simeq 0.07[v_{thi}/L_n] \simeq 0.58\gamma_{max}(\rho^* = 1/180)$. The situation in the TEM regime is however different. Figure 3(*a*) shows the k_θ-spectrum of the collisionless TEM growth rate γ, for the TEM CYCLONE case ($\rho^* = 1/180$), the TEM TCV case ($\rho^* = 1/80$) and a small TEM CYCLONE case ($\rho^* = 1/60$), considering $T_e = T_i$ and the hybrid model for electrons. Peaked gradient profiles described by equation (22) with $\Delta_A = 0.2a$ are used here. Although the
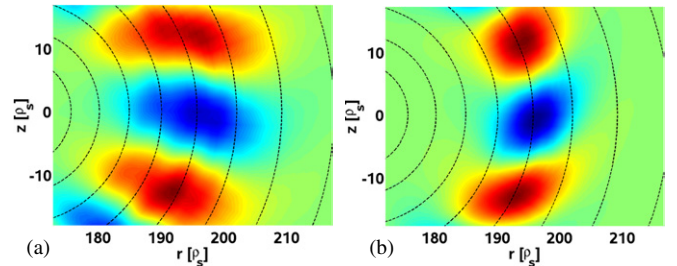
Figure 4. Linear structure of the mode $k_\theta\rho_s = 0.3$, in the poloidal plane, for (*a*) an ITG-dominated regime and (*b*) a TEM-dominated regime in a small plasma ($\rho^* = 1/60$) considering $T_e = T_i$. TEM instabilities are more radially localized than ITG instabilities.

plasma size is different for each case, the linear growth rates appear to be only slightly reduced in a smaller plasma. This observation can be explained by the radial extension scaling of linear TEM modes. While the radial extension of ITG modes Δr_{ITG} scales as $\Delta r_{ITG}/\rho_s \sim 1/\sqrt{\rho^*}$ or $\Delta r_{ITG}/a \sim \sqrt{\rho^*}$ [34–36], we observe that the radial extension of TEM modes Δr_{TEM} scales as $\Delta r_{TEM}/\rho_s \sim 1/\rho^*$ or $\Delta r_{TEM}/a \sim$ constant. For the mode $k_\theta\rho_s = 0.3$ corresponding to the TEM CYCLONE case, the radial extension $\Delta r_{TEM}/a \simeq 0.2$ is found for all ρ^* values considered. The TEM modes are thus more radially localized in a small plasma, as illustrated in figure 4, leading to weaker profile shearing effects [37] due to finite plasma size and hence to a weaker reduction in growth rates compared with the ITG case. In addition, results of collisional linear simulations, accounting for both electron–ion and electron–electron collisions with
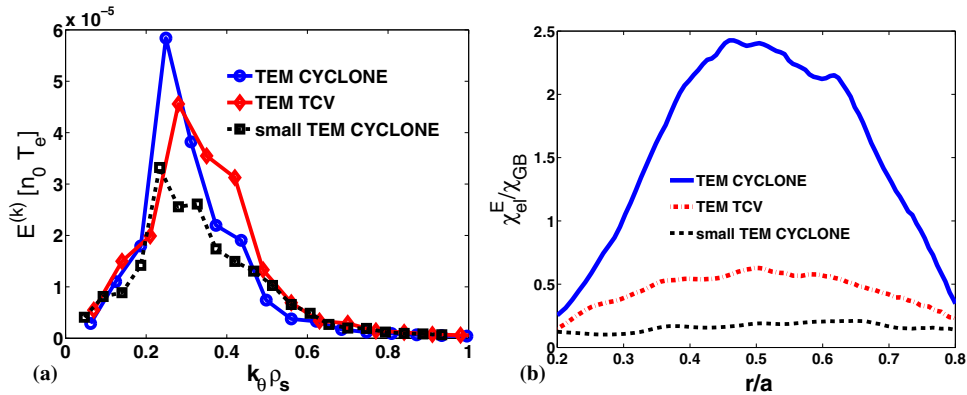
Figure 5. (*a*) Turbulence energy spectra averaged between $t = 1000[a/c_s]$ and $t = 1100[a/c_s]$ and (*b*) electron energy diffusivity profile $\chi_{el}^E(r)$ averaged between $t = 800[a/c_s]$ and $t = 950[a/c_s]$, for the TEM CYCLONE case ($\rho^* = 1/180$), the TEM TCV case ($\rho^* = 1/80$) and a small TEM CYCLONE case ($\rho^* = 1/60$), considering $T_i = T_e/2$. Important non-linear finite-ρ^*-effects regarding the electron energy transport are observed, the diffusivity in gyro-Bohm units being significantly reduced in smaller plasmas (similarly to the ITG regime behaviour).

collisionality $\nu_{ei}a/v_{thi} = 5 \times 10^{-3}$, are shown in figure 3(*b*) and provide the same trend as the collisionless case regarding the plasma finite-size-effects, i.e. weak ρ^* effects. Consistent with results obtained in section 9, the linear growth rates are reduced by collisions through the electron detrapping process, regardless of the considered wavelength or plasma size. Note that, as mentioned in section 3, different temperature and density profile shapes are used for linear and non-linear simulations, which could provide different sensitivities to finite-ρ^*-effects. In order to address this issue and further pursue the study of finite-ρ^*-effects in linear TEM simulations, the TEM CYCLONE case is again considered, this time with $T_i = T_e/3$ and using the wide gradient temperature and density profiles as given by equation (21), the same profiles as for non-linear simulations. The growth rate of the mode $k_\theta \rho_s = 0.5$ is found to be $\gamma(\rho^* = 1/180) \simeq 0.27[c_s/L_n]$. The same simulation is repeated for $\rho^* = 1/60$, i.e. corresponding to a small TEM CYCLONE case. The obtained growth rate, $\gamma(\rho^* = 1/60) \simeq 0.24[c_s/L_n]$, is only marginally reduced ($\sim 10\%$) with respect to the TEM CYCLONE growth rate, which confirms the weak ρ^* effects in linear temperature-gradient-driven TEM simulations.

Considering again the TEM CYCLONE case, the TEM TCV case and a small TEM CYCLONE case ($\rho^* = 1/60$), non-linear collisionless simulations of turbulence using the hybrid electron model are performed for $T_i = T_e/2$ (the chosen temperature ratio aiming at stabilizing the ETG modes), and using the Krook operator in order to control the numerical noise ($\gamma_k \sim 0.03[c_s/a]$). The turbulence energy spectra, averaged between $t = 1000[a/c_s]$ and $t = 1100[a/c_s]$, are similarly shaped but exhibit a turbulence level depending on the plasma size, as shown in figure 5(*a*). The electron energy diffusivity χ_{el}^E in gyro-Bohm units, averaged between $t = 800[a/c_s]$ and $t = 950[a/c_s]$, is much larger for the largest plasma case, i.e. the TEM CYCLONE case, as presented in figure 5(*b*). The TEM-related turbulent electron transport reduction through finite-ρ^*-effects is thus of the same order as observed for ion transport in the ITG regime, i.e. a reduction in corresponding diffusivities by a factor of ~ 4 when going from $\rho^* = 1/180$ to $\rho^* = 1/80$ (see also figure 1 of [23]). As shown in figure 5(*b*),

going from $\rho^* = 1/180$ to $\rho^* = 1/60$ reduces the electron energy diffusivity of the TEM CYCLONE case by a factor ~ 10 in gyro-Bohm units. In contrast to the ρ^* effects in the linear TEM regime, the ρ^* effects in the non-linear TEM regime thus appear to be important (regarding the turbulent transport), in agreement with [13].

7. Effects of axisymmetric modes on temperature-gradient-driven TEM turbulence

The axisymmetric electric fields, corresponding to the toroidal Fourier mode $n = 0$, and associated zonal flows are a well-established mechanism for ITG turbulence saturation [26, 38]. In the TEM regime, the effects of zonal flows on the saturation mechanism turn out to be less obvious. [8, 9] claim that zonal flows do not contribute significantly to the TEM saturation mechanism for $\eta_e = \nabla \ln T_e / \nabla \ln n_e > 1$, i.e. for mainly temperature-gradient-driven TEM turbulence. This assertion is confirmed in [6], where only a limited role of zonal flows in TEM turbulence simulations is observed for the TEM CYCLONE case with both $T_i = T_e$ and $T_i = T_e/3$. Here, additional confirmation regarding the latter conclusions is provided through new collisionless simulations (within the frame of the hybrid model) of the pure temperature-gradient-driven TEM turbulence case described in section 3, for which $\eta_e = 4.75$. Figure 6 shows the electron energy diffusivity profile $\chi_{el}^E(r)$ averaged between $t = 1000[a/c_s]$ and $t = 1800[a/c_s]$, for both cases where the toroidal Fourier mode $n = 0$ is retained or not in the simulation. The transport level is clearly only marginally affected by the presence of zonal flows, in contrast to the transport level in the ITG regime which is largely reduced in the presence of zonal flows. The Krook operator is used both for ions and electrons, with $\gamma_k \sim 0.01[c_s/a]$ significantly smaller than the maximum linear growth rate $\gamma_{max} \sim 0.07[c_s/a]$ of the most unstable TEM.

8. Varying the ETG in the TEM regime

In this section, a comparison between linear and non-linear ETG scans is performed, considering the collisionless TEM
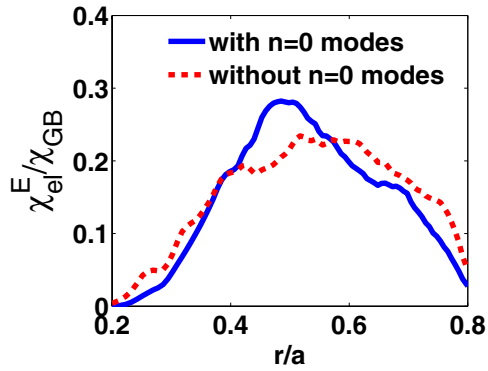
Figure 6. Effects of axisymmetric Fourier modes ($n = 0, m$) on electron transport level in the temperature-gradient-driven TEM regime (pure TEM case described in section 3). Electron energy diffusivity profile $\chi_{el}^E(r)$ averaged between $t = 1000[a/c_s]$ and $t = 1800[a/c_s]$. Regarding the averaged turbulent transport level, no clear effect of zonal flows is visible in the temperature-gradient-driven TEM regime.

CYCLONE case with $T_i = T_e/2$ along with the wide gradient density and temperature profiles (equation (21)). The Krook operator is used for controlling the numerical noise, both for electrons and ions. Note that the relaxation rate γ_k does vary according to the maximum linear growth rate γ_{max} of the considered system, i.e. according to the ETG. An approximately constant ratio $\gamma_k/\gamma_{max} \simeq 0.15$ is chosen throughout this section.

In the ITG regime, there is a well-established difference between the collisionless linear and non-linear critical ITGs, the so-called Dimits shift [29]: due to the shearing effects of zonal flows, a temperature gradient which provides a linear unstable ITG mode might be unable to sustain a non-vanishing turbulent transport if the corresponding maximum linear growth rate γ_{max} is of the order of the averaged $\vec{E} \times \vec{B}$ shearing rate $\langle |\omega_{E \times B}| \rangle_r$. For a finite turbulence level to persist, the ITG should provide a maximum growth rate γ_{max} that is clearly larger than the maximum possible zonal flow shearing rate, limited by Kelvin–Helmoltz-like instabilities: $\gamma_{max} > \langle |\omega_{E \times B}| \rangle_r$ [26, 39].

The situation in the temperature-gradient-driven TEM regime turns out to be different, as shown in figure 7 obtained with the TEM CYCLONE case parameters. Considering low ETGs ($a/L_{Te} \lesssim 1.5$), which provide marginally unstable linear TEM instabilities, a non-vanishing turbulent transport level is obtained in non-linear simulations. Both the linear growth rates γ_{max} and the non-linear turbulent diffusivities χ_{el}^E appear to scale linearly with the ETG (the drive of turbulence) and to have approximately the same critical gradient ($a/L_{Te} \simeq 1$), in contrast to the ITG regime where ITGs in the so-called Dimits shift region give rise to linear instabilities but cannot maintain a finite turbulent transport as a result of the shearing of turbulence by zonal flows [38]. Note that a finite level of electron energy transport is found even for ETGs at which $\gamma_{max} \simeq \langle |\omega_{E \times B}| \rangle_r$, in contrast to the ITG regime situation. This illustrates the limited effects of zonal flows on temperature-gradient-driven TEM turbulence, as already discussed in section 7.

A convergence check is performed for a particular case addressed in this section, i.e. considering the ETG $a/L_{Te} = 2.484$. Increasing the electron marker number by a factor 2, i.e. considering 200×10^6 electron markers, and reducing the relaxation rate by a factor 2, i.e. considering $\gamma_k \simeq 0.015[c_s/a]$, provides an electron energy diffusivity of $\chi_{el}^E/\chi_{GB} \simeq 2.1$, averaged between $r/a = 0.4$ and $r/a = 0.6$. The latter value is within the typical uncertainty range of 15% [22] regarding the diffusivity $\chi_{el}^E/\chi_{GB} \simeq 2.35$, obtained with 100×10^6 electron markers and $\gamma_k \simeq 0.03[c_s/a]$ and shown in figure 7(b). Note that the signal/noise ratio, i.e. the energy of the nearly field-aligned Fourier modes divided by the energy of the unphysical, non-field-aligned Fourier modes, is satisfactory for both simulations (above 50). The latter result thus provides confidence as to the convergence of the presented TEM non-linear results.

9. Linear and non-linear collisional effects in the TEM regime

While ion collisions tend to non-linearly increase the ITG turbulence through zonal flow damping [26, 40], electron collisions have a strong and mostly linear effect on temperature-gradient-driven TEM instabilities, actually reducing the TEM drive through the electron detrapping process they generate. The most obvious collisional effect is thus the reduction in the TEM linear growth rates with increasing collisionality. The TEM TCV case is chosen for illustrating this latter fact, considering the following modified gradients: $a/L_{Ti} = 0$, $a/L_{Te} = 1.70$, $a/L_n = 0.85$ which provide an essentially pure TEM regime. Figure 8(a) shows the dependence on electron collisionality ν_{ei} of the linear growth rate γ corresponding to the mode $k_\theta \rho_{Li} = 0.4$, for different temperature ratios T_e/T_i and collision operators. As expected, neglecting electron–electron collisions (electron–ion collisions only) leads to a weaker collisional growth rate reduction. Note that the collisional reduction in the growth rates is in accordance with numerical results obtained in [41] using the flux-tube version of the gyrokinetic code GEM. The collisionality ν_{ei} is normalized with respect to the real frequency of the mode at zero collisionality $\omega(\nu_{ei} = 0)$, i.e. $\omega(\nu_{ei} = 0) \simeq 0.54[v_{thi}/a]$ for $T_i = T_e/3$ and $\omega(\nu_{ei} = 0) \simeq 0.38[v_{thi}/a]$ for $T_i = T_e/2$. Note that ω remains essentially unaffected by electron collisions.

A small TEM CYCLONE case, i.e. the TEM CYCLONE case described in section 3 with $\rho^* = 1/60$, is chosen in order to address the difference between linear and non-linear collisional effects on temperature-gradient-driven TEM instabilities. The temperature ratio $T_i = T_e/3$ is considered. The collisional reduction in the maximum linear growth rate γ_{max} (corresponding to the mode $k_\theta \rho_{Li} = 0.3$) with increasing electron–ion collision frequency ν_{ei} is shown in figure 8(b) and compared with the collisional damping of the quasi-stationary electron turbulent energy flux Q_{el}, averaged between $r/a = 0.4$ and $r/a = 0.6$. The reduction of non-linear turbulent transport (compared with a collisionless case) turns out to be stronger than the reduction in the linear growth rate and can thus not be explained by a simple mixing length
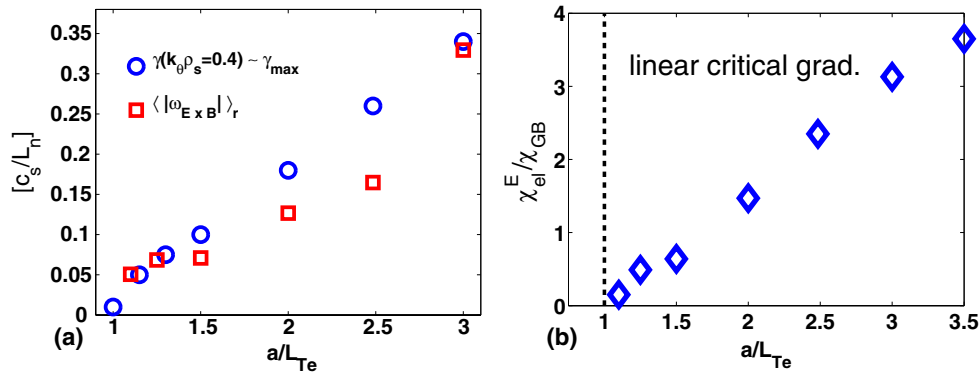
Figure 7. Electron temperature gradient a/L_{Te} dependence of (*a*) the maximum TEM linear growth rate γ_{max} and the radial average of the absolute value of the $\vec{E} \times \vec{B}$ shearing rate $\langle|\omega_{E\times B}|\rangle_r$ (averaged between $r/a = 0.4$ and $r/a = 0.6$), and (*b*) the electron energy diffusivity χ_{el}^E, averaged between $r/a = 0.4$ and $r/a = 0.6$ and over a time window of $\Delta t \sim 300[a/c_s]$, in the quasi-stationary state of the simulation ($t \sim 1000[a/c_s]$). Linear and non-linear critical temperature gradients are obviously essentially identical ($a/L_{Te} \simeq 1$).
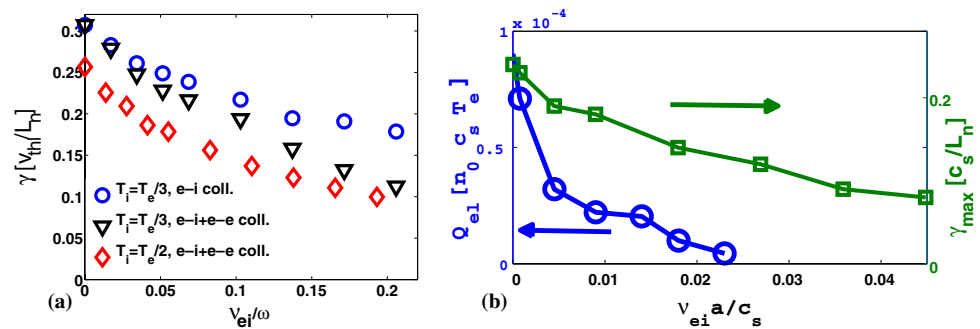
Figure 8. (*a*) Collisional damping of linear growth rates in the TEM regime. The TEM TCV case with $a/L_{Ti} = 0$, $a/L_{Te} = 1.70$, $a/L_n = 0.85$, mode $k_\theta \rho_{Li} = 0.4$. The electron–ion collision frequency ν_{ei} is normalized with respect to ω, the collisionless real frequency of the considered mode $k_\theta \rho_{Li} = 0.4$. (*b*) The small TEM CYCLONE case, $T_i = T_e/3$. Electron collisionality scan, both for the quasi-stationary electron turbulent energy flux Q_{el}, averaged between $r/a = 0.4$ and $r/a = 0.6$, and for the maximum linear growth rate γ_{max}. Electron collisions have a damping effect on TEM instabilities both in linear and non-linear simulations, the damping of non-linear turbulent transport (compared with a collisionless case) being however stronger than the damping of linear growth rates.

argument $\chi \sim \gamma_{max}/\langle k_\perp^2 \rangle$. Note that the real frequency of the mode $k_\theta \rho_{Li} = 0.3$, $\omega \simeq 0.48[c_s/L_n]$, remains essentially unaffected by collisions, and that both electron–ion and electron–electron collisions are accounted for. The non-linear runs for simulating collisional TEM turbulence presented in figure 8(*b*) are actually very challenging due to the large number of markers required ($\sim 600 \times 10^6$ electrons and $\sim 200 \times 10^6$ ions) combined with the small time step related to electron dynamics, leading to $\sim 500\,000$ CPU hours consumed for each simulation.

Considering again the small TEM CYCLONE case with $T_i = T_e/3$, figure 9 shows the turbulent component (in the poloidal plane) of the perturbed electrostatic potential, $e(\phi - \langle\phi\rangle_S)/T_{e0}$, at $t = 1000[a/c_s]$ for the two collisionalities $\nu_{ei}a/c_s(r/a = 0.5) = 7.5 \times 10^{-4}$ and $\nu_{ei}a/c_s(r/a = 0.5) = 4.5 \times 10^{-3}$. As expected, the averaged turbulence level is weaker for a stronger collisionality. Note that the collisionality dependence on density and temperature profiles is accounted for in ORB5 simulations, leading in fact to stronger collisionality close to the plasma edge and weaker collisionality close to the magnetic axis. The collisionality increase towards the edge is explained by a weaker reduction in collisionality due to lower density ($\sim n$) than the increase of collisionality due to lower temperature ($\sim T_e^{-3/2}$). Compared

with the weakly collisional situation, the TEM turbulence in the case of stronger collisionality is thus more reduced and even quenched when going towards the plasma edge as illustrated in figure 9.

10. Conclusions

In this paper, results from global gyrokinetic simulations of temperature-gradient-driven TEM turbulence performed with the ORB5 code are discussed. Two different methods for controlling the numerical noise (inherent to the PIC approach) are evaluated and compared. A linear benchmark in the TEM regime against the Eulerian gyrokinetic code GENE is presented (accounting for fully kinetic electron response), which shows good agreement between both codes. The GENE–ORB5 comparison, however, points out the limitations of the polarization drift term in the quasi-neutrality equation considered only to second order in $k_\perp \rho_L$ in ORB5. While the long wavelength approximation is valid for computing electron heat fluxes with the parameters considered in this paper, it is nonetheless a limiting factor of the ORB5 code if one intends to explore a larger range of parameters and is therefore currently being addressed through the implementation of an integral
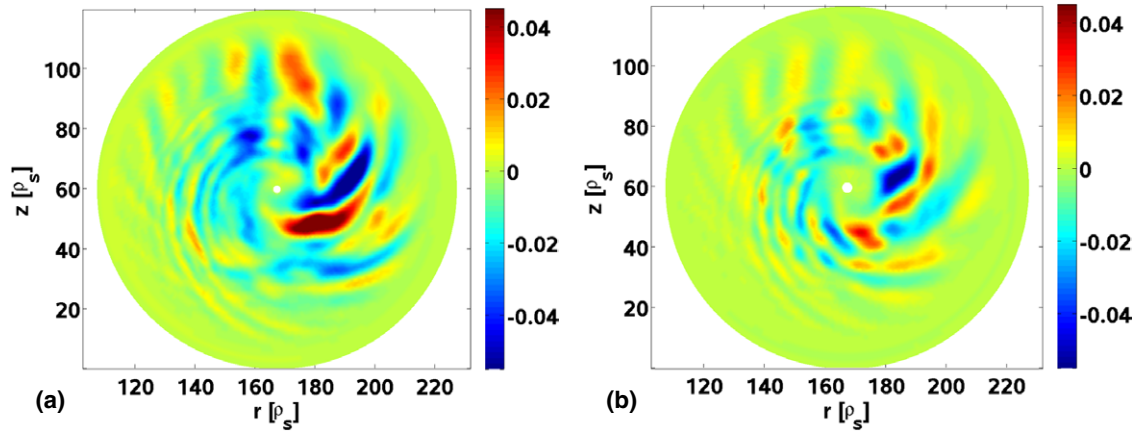
Figure 9. Small TEM CYCLONE case, $T_i = T_e/3$. Poloidal cross-section of the non-zonal component of the electrostatic potential $e(\phi - \langle\phi\rangle_S)/T_{e0}$ at $t = 1000[a/c_s]$ for the two collisionalities (*a*) $\nu_{ei}a/c_s(r/a = 0.5) = 7.5 \times 10^{-4}$ and (*b*) $\nu_{ei}a/c_s(r/a = 0.5) = 4.5 \times 10^{-3}$. The turbulence reduction through electron collisions is clearly visible.

form of the polarization drift operator valid to all orders in $k_\perp\rho_L$ [42].

The effects of finite plasma size on TEM instabilities turn out to be important in the non-linear regime, while there is almost no effect of finite plasma size in the TEM linear regime. Note the difference compared with ITG-dominated cases, where the effects of finite plasma size are important both in linear and non-linear regimes.

In the temperature-gradient-driven TEM regime, the zonal flows are shown to play no role in turbulence saturation, confirming previous studies. Accordingly, no Dimits shift region is observed in this regime, unlike in the ITG regime that features a Dimits shift region as a consequence of the importance of zonal flow shearing in turbulence saturation.

Electron collisions are found to reduce both the linear growth rate and the transport level related to TEM instabilities, through the electron detrapping process. Note that, in contrast, the ion collision effects on ITG turbulence are almost fully non-linear and lead to a general increase in ITG turbulence level through zonal flow damping [26, 40].

Acknowledgments

References

[1] Falchetto G L, Vaclavik J and Villard L 2003 *Phys. Plasmas* **10** 1424–36
[2] Waltz R E, Austin M E, Burrell K H and Candy J 2006 *Phys. Plasmas* **13** 052301
[3] Chowdhury J, Ganesh R, Angelino P, Vaclavik J, Villard L and Brunner S 2008 *Phys. Plasmas* **15** 072117
[4] Bottino A, Peeters A G, Sauter O, Vaclavik J, Villard L and Team A U (ASDEX Upgrade Team) 2004 *Phys. Plasmas* **11** 198–206
[5] Bottino A, Sauter O, Camenen Y and Fable E 2006 *Plasma Phys. Control. Fusion* **48** 215
[6] Jolliet S 2009 Gyrokinetic particle-in-cell global simulations of ion-temperature-gradient and collisionless-trapped-electron-mode turbulence in tokamaks *PhD Thesis* Ecole polytechnique fédérale de Lausanne
[7] Lee W 1987 *J. Comput. Phys.* **72** 243–69
[8] Dannert T and Jenko F 2005 *Phys. Plasmas* **12** 072309
[9] Ernst D R, Lang J, Nevins W M, Hoffman M, Chen Y, Dorland W and Parker S 2009 *Phys. Plasmas* **16** 055906
[10] Xiao Y, Holod I, Zhang W, Klasky S and Lin Z 2010 *Phys. Plasmas* **17** 022302
[11] Lang J, Parker S E and Chen Y 2008 *Phys. Plasmas* **15** 055907
[12] Merz F and Jenko F 2008 *Phys. Rev. Lett.* **100** 035005
[13] Xiao Y and Lin Z 2009 *Phys. Rev. Lett.* **103** 085004
[14] Scott B and Smirnov J 2010 *Phys. Plasmas* **17** 112302
[15] Görler T, Lapillonne X, Brunner S, Dannert T, Jenko F, Merz F and Told D 2011 *J. Comput. Phys.* **230** 7053–71
[16] Tran T M, Appert K, Fivaz M, Jost G, Vaclavik J and Villard L 1999 *Theory of Fusion Plasmas, Int. Workshop (Bologna Editrice Compositori, Società Italiana di Fisica)* p 45
[17] Jolliet S, Bottino A, Angelino P, Hatzky R, Tran T, McMillan B, Sauter O, Appert K, Idomura Y and Villard L 2007 *Comput. Phys. Commun.* **177** 409–25
[18] Lin Z, Tang W M and Lee W W 1995 *Phys. Plasmas* **2** 2975–88
[19] Brunner S, Valeo E and Krommes J A 1999 *Phys. Plasmas* **6** 4504–21
[20] Vernay T, Brunner S, Villard L, McMillan B F, Jolliet S, Tran T M, Bottino A and Graves J P 2010 *Phys. Plasmas* **17** 122301
[21] Hahm T S 1988 *Phys. Fluids* **31** 2670–3
[22] McMillan B F, Jolliet S, Tran T M, Villard L, Bottino A and Angelino P 2008 *Phys. Plasmas* **15** 052308
[23] McMillan B F, Lapillonne X, Brunner S, Villard L, Jolliet S, Bottino A, Görler T and Jenko F 2010 *Phys. Rev. Lett.* **105** 155001
[24] Lapillonne X, McMillan B F, Görler T, Brunner S, Dannert T, Jenko F, Merz F and Villard L 2010 *Phys. Plasmas* **17** 112321
[25] Chen Y and Parker S E 2007 *Phys. Plasmas* **14** 082301
[26] Vernay T, Brunner S, Villard L, McMillan B F, Jolliet S, Tran T M and Bottino A 2012 *Phys. Plasmas* **19** 042301

[27] Lapillonne X, Brunner S, Dannert T, Jolliet S, Marinoni A, Villard L, Görler T, Jenko F and Merz F 2009 *Phys. Plasmas* **16** 032308
[28] Hahm T S 1994 *Phys. Plasmas* **1** 2940–2944
[29] Dimits A M *et al* 2000 *Phys. Plasmas* **7** 969–983
[30] Bottino A 2004 Modelling of global electrostatic microinstabilities in tokamaks: effects of $E \times B$ flow and magnetic shear *PhD Thesis* Ecole polytechnique fédérale de Lausanne
[31] Merz F and Jenko F 2010 *Nucl. Fusion* **50** 054005
[32] Lin Z, Ethier S, Hahm T S and Tang W M 2002 *Phys. Rev. Lett.* **88** 195004
[33] Candy J, Waltz R E and Dorland W 2004 *Phys. Plasmas* **11** L25–8
[34] Romanelli F and Zonca F 1993 *Phys. Fluids B: Plasma Phys.* **5** 4081–9

[35] Brunner S, Fivaz M, Tran T M and Vaclavik J 1998 *Phys. Plasmas* **5** 3929–49
[36] Garbet X, Idomura Y, Villard L and Watanabe T 2010 *Nucl. Fusion* **50** 043002
[37] Waltz R E, Candy J M and Rosenbluth M N 2002 *Phys. Plasmas* **9** 1938–46
[38] Lin Z, Hahm T S, Lee W W, Tang W M and White R B 1998 *Science* **281** 1835–7
[39] Waltz R E, Dewar R L and Garbet X 1998 *Phys. Plasmas* **5** 1784–92
[40] Lin Z, Hahm T S, Lee W W, Tang W M and Diamond P H 1999 *Phys. Rev. Lett.* **83** 3645–8
[41] Lang J, Chen Y and Parker S E 2007 *Phys. Plasmas* **14** 082315
[42] Mishchenko A, Könies A and Hatzky R 2005 *Phys. Plasmas* **12** 062305